



Microstructure and mechanical properties of cold sprayed 7075 deposition during non-isothermal annealing



M.R. Rokni ^{a,*}, C.A. Widener ^a, V.K. Champagne ^b, G.A. Crawford ^{a,*}

^a Department of Materials & Metallurgical Engineering, Advanced Materials Processing Center, South Dakota School of Mines & Technology (SDSMT), SD, USA

^b U.S. Army Research Laboratory, Weapons and Materials Research Directorate, Aberdeen Proving Ground, MD, USA

ARTICLE INFO

Article history:

Received 2 June 2015

Revised 8 July 2015

Accepted in revised form 9 July 2015

Available online 15 July 2015

Keywords:

Aluminum alloys

Cold spraying

Non-isothermal

Annealing

TEM

ABSTRACT

This study presents microstructure and mechanical property relationships of cold-sprayed 7075 aluminum during non-isothermal annealing. Microstructure evolution during non-isothermal annealing from room temperature to 450 °C was performed using in-situ heating via a hot-stage transmission electron microscope. Additional characterization was performed using differential scanning calorimetry and X-ray diffraction. Grain size, dislocation density, microstrain, lattice parameter, and precipitation phenomena were evaluated as a function of annealing temperature. The results showed that cold spray processing accelerated the precipitation kinetics of strengthening phases in the microstructure, compared to the as-received cold spray powder, but did not affect the overall precipitation sequence. Also, pancaked grain structures, found at particle–particle interfaces within the deposition, were converted, due to recrystallization, to ultrafine-grained structures during annealing. The ultrafine-grained structures experienced limited grain growth during the annealing process. This was attributed to the nucleation of grain boundary precipitates in the as-sprayed material, primarily originating from grain boundary solute segregation present in the cold spray powder. Mechanical properties were evaluated using microhardness testing, after annealing, and correlated with microstructural analysis. When subjected to low temperature annealing (below 370 °C), the cold spray processed material had a lower microhardness than that found in conventional 7075 aluminum subjected to the same thermal treatment, due to the presence of inter-particle porosity in the cold spray microstructure. Annealing at temperatures above 370 °C, however, resulted in an increase in hardness, likely due to a reduction in inter-particle porosity and grain boundary strengthening associated with the retention of an ultrafine grain structure at high temperatures.

© 2015 Elsevier B.V. All rights reserved.

1. Introduction

Cold spray processing is a material deposition process which achieves a dense coating or bulk deposition through extensive plastic deformation of fine powder particles upon impact with a target substrate [1–4]. Here small particles (~5 to 50 μm), in the solid state, are propelled towards a substrate at high velocity (typically 300 to 1200 m/s), subsequently developing a solid deposit as a consequence of the particles' kinetic energy on impact [3–6]. Although the deposition process relies on plastic deformation of the powder particles, the plastic strain experienced by the particles is non-uniform and it is well established that the microstructure of the deposited coating is also non-uniform [2,3,5–8]. For instance, several reports have shown the presence of both micron and sub-micron sized grains within the cold-spray deposition. The majority of these reports, however, have been focused on pure metals (e.g. Al [3,4], Ti [5], Cu [1,9], and Ni [10,11]), with few studies [6,7,12–14] examining the microstructure of CSP industrial alloys. With this in mind, among its many applications, cold spray processing has gained significant attention

for its potential to perform dimensional restoration and repair of damaged metallic components (e.g. aircraft parts). Thus, there is a need for improved understanding regarding the use of cold spray processing for deposition of industrial alloys.

Recently, Rokni et al. [12] reported on the microstructure and local mechanical behavior of cold spray deposited 7075 aluminum (Al) alloys. Results showed the presence of both micro-scale grains in particle interiors and ultra-fine grained (UFG) structures at particle–particle boundaries. The presence of UFG structures have also been reported in CS processed (CSP) depositions in other materials (e.g. Al [3,15], Ti [5], Cu [11], and Ni [16]). Furthermore, it has been widely reported that the majority of grain boundaries (GBs) within UFG structures formed during severe plastic deformation (SPD) processes are in a non-equilibrium state due to the accumulation of large amounts of dislocations [7,17–21]. As a result, the GBs are thermally unstable, and grain growth may occur easily at moderate temperatures, leading to a variation in mechanical properties. Considering that CSP depositions may be used in applications where the parts experience moderate to high temperatures for extended periods of time, it is important to understand the thermal stability of the CSP microstructure. Furthermore, many of the conventional aluminum alloys, for which CSP deposition may be used, are precipitation hardenable alloys (e.g. 6061 Al and

* Corresponding authors.

E-mail addresses: reza.rokni@mines.sdsmt.edu, mreza.rokni@gmail.com (M.R. Rokni), grant.crawford@sdsmt.edu (G.A. Crawford).

7075 Al). Thus, it is important to understand the influence of cold spray on the precipitation of strengthening phases within the microstructure during heating.

The microstructural evolution of Al–Mg–Zn (similar to 7075 Al) alloys subjected to severe plastic deformation (equal channel angular extrusion (ECAP) [22], high pressure torsion (HPT) [23], cryomilling and hot isostatic pressing/extrusion [24]) and subsequent heat treatment has been reported. Results show that SPD processes, resulting in UFG structures, alter the precipitation kinetics of strengthening phases (MgZn_2 , η'/η) in the microstructure [22–24]. Furthermore, the studies highlight that these materials are strengthened by not only precipitate strengthening mechanism, but also, and more importantly, by grain boundary strengthening due to the presence of the UFG structure after thermal treatment [24]. A subtle difference between these studies and the CSP microstructure is the significant non-uniformity observed in as-deposited CSP microstructures, i.e. microscale grains in particle interiors and UFG structures located at particle–particle boundaries. Furthermore, several reports have demonstrated the presence of extensive grain boundary solute segregation in both gas atomized cold spray powder and CSP depositions [12,17,25–27]. The thermal stability of UFG structures can be maintained, to some extent, by the nucleation of fine, incoherent precipitates at the GBs so that GB migration causing grain growth is hindered by the pinning effect of these precipitates [28–30]. Thus, it is important to develop an understanding of the microstructural and mechanical property evolution of CSP 7075 Al during thermal treatment.

In this work, the microstructural and mechanical property evolution of CSP 7075 Al are reported during non-isothermal annealing from room temperature to 450 °C. Specific attention has been devoted to studying both the precipitation and restoration processes in the microstructure. In-situ hot-stage transmission electron microscopy (TEM), differential scanning calorimetry (DSC), and X-ray diffraction (XRD) were used to monitor the changes in the CSP microstructure (i.e. grain size, dislocation density, microstrain, lattice parameter, and precipitation sequence) during heating. Furthermore, Vickers microhardness was performed to correlate observed microstructure changes with resulting mechanical behavior.

2. Experimental procedure

2.1. Coating preparation

7075 aluminum (Al) (Al-6.09 Zn-2.68 Mg-1.28Cu-0.18Fe-0.13 wt.% Si) coatings were produced using commercially available gas-atomized 7075 Al powder (Valimet, Stockton, CA, USA), $18.6 \pm 8.2 \mu\text{m}$ in size. Feedstock powder size was measured using a laser diffraction particle size analyzer (Microtrac s3000, Microtrac Software Co., USA). Cold spray deposition was performed using a VRC Gen III high-pressure cold spray system (VRC Metal Systems, Rapid City, SD, USA). Deposition was carried out onto wrought 7075 Al substrates using helium process gas while maintaining a gas pressure of 2.8 MPa and temperature of 400 °C at the heater exit. Coatings were deposited using a nozzle stand-off distance of 25 mm, deposition angle of 90°, powder feed rate of 12 g min^{-1} , and a nozzle traveling speed of 600 mm s^{-1} . Finally, a total deposition thickness of $\sim 8.5 \text{ mm}$ was achieved in this study.

2.2. Non-isothermal annealing

The annealing behavior of the cold spray deposited material was characterized by continuous in-situ heating of the sample to 450 °C in 45 min (10°C/min) from ambient temperature using the TEM heating stage followed by microstructural characterization. A custom software code was written to capture a TEM image of the microstructure every 7 s. A total of 420 TEM images were combined to generate a video, which documented the microstructural evolution throughout the non-isothermal annealing process (RT to 450 °C). The video has been provided

as a supplemental file (Video) with this publication. For this purpose, thin disks, 3 mm in diameter, were excised from perpendicular direction to the particle impact vector of the deposition, and then polished, dimpled, and ion milled for 4 h.

2.3. Thermal analysis

Thermal analysis was performed in a DSC machine (SDT Q600, TA Instruments, DE, USA) to investigate the precipitation sequence of the CSP 7075 deposition and the as-received powder during annealing process. The DSC was calibrated by using standard samples, giving an accuracy of $\pm 0.3^\circ\text{C}$ for the temperature and $\pm 0.02 \text{ mW}$ for the heat flow measurements. Polished alloy disks with a diameter of 3 mm were sealed in aluminum pans and heated in a flowing Argon atmosphere at the same heating rate used in the TEM (10°C/min). An empty cup was used as a reference to serve as a base line in this study.

2.4. Microstructure characterization

The microstructure of the as-received 7075 powder (ARP sample) and CSP 7075 Al deposition (CSP sample) annealed at various temperatures was evaluated by TEM, scanning electron microscopy (SEM), and XRD. TEM micrographs were obtained by utilizing a JEM-2100 LaB₆ operating at 200 kV. Thin disks of 3 mm diameter were excised from the deposition, and then polished, dimpled, and ion milled for 4 h. The grain size measurements were carried out particle–particle interfaces with panned structure using TEM analysis. 100 TEM grain size measurements were made at each temperature and the average and standard deviation are reported.

XRD experiments were performed using a D8 Bruker diffractometer (Bruker AXS, Karlsruhe, Germany) with negligible instrumental broadening using $\text{Cu K}\alpha_1$ radiation in the range $2\theta = 35\text{--}105^\circ$ with a step size of 0.02° and counting time of 1 s per step. The XRD results were also used to calculate the mean grain diameter, d , and microstrain, ε , of the CSP samples at RT and following annealing at various critical temperatures. These values were calculated using Eq. (1) [24,31]:

$$B \cos \theta_B = \frac{K\lambda}{d} + \varepsilon \sin \theta_B, \quad (1)$$

where λ is the wavelength of $\text{Cu K}\alpha_1$ radiation, i.e. 1.54 \AA is ~ 0.9 , ε is the microstrain, θ_B is the Bragg angle, and B is the peak broadening term. The values of d and ε were obtained from the slope and intercept of the $B \cos \theta_B$ vs. $\sin \theta_B$ curve by performing a linear regression analysis. Additionally, following the Williamson–Hall method [32], the full width at half-maximum (FWHM) values were used to calculate peak broadening, B , which was derived from Eq. (2):

$$\sqrt{B_{\text{obs}}^2 - B_{\text{inst}}^2}, \quad (2)$$

where B_{obs} is the observed peak broadening and B_{inst} is the instrumental broadening.

2.5. Mechanical property evaluation

Microhardness measurements were performed using a Vickers microhardness tester (HVM-2, Shimadzu, Tokyo, Japan) with a load of 300 gf and a loading time of 10 s. The indenter was the Vickers diamond pyramid. For all the microhardness values reported in this paper 10 measurements have been carried out and the standard deviations have been calculated based on the obtained data.

3. Results and discussion

3.1. Microstructure evaluation — as-received 7075 Al powder

Fig. 1 shows SEM images of the as-received 7075 Al powder (ARP) prior to cold spray deposition. Fig. 1a shows a typical powder particle characterized by a spherical morphology and diameter of roughly 20 μm . The powder particle is also surrounded by multiple micro-satellite particles (less than 5 μm in size). Examining the surface of the powder particles reveals an external grain structure with grain size of $\sim 1\text{--}3\text{ }\mu\text{m}$. Fig. 1b shows a back-scatter electron (BSE) image cross-section of the as-received powder, prepared by metallographic polishing in an epoxy resin. The internal structure is characterized by a cellular grain structure with significant solute segregation at grain boundaries, evidenced by the sharp atomic number contrast in the BSE image. The presence of solute segregation in gas-atomized cold spray powder has been discussed elsewhere [12].

3.2. Microstructure evaluation — CSP deposition in as-deposited condition

Fig. 2 shows TEM micrographs obtained from the CSP 7075 Al deposition (CSP sample) in as-deposited condition. Fig. 2a shows a montage image obtained from a characteristic region of the CSP sample. The montage image is composed of 20 individual scanning TEM (STEM) images. From inspection of Fig. 2a, powder particles have experienced significant plastic deformation resulting in a uniform and high quality cold spray deposition. There is, however, some evidence of porosity, triple junction voids, and lack of bonding between powder particles. The red arrow in Fig. 2a shows an elongated void located at a particle/particle boundary. It is important to note that although the coating quality is good, even limited porosity can have a detrimental effect on the final mechanical properties of CSP depositions [33–37]. This topic will be discussed further in Section 3.4.4.

From inspection of Fig. 2a, three regions are clearly distinguishable in the as-sprayed microstructure: (1) particle interior regions, Fig. 2b; (2) particle–particle interface regions containing pancake grain structures, Fig. 2c; and (3) particle–particle interface regions containing an ultra-fine grain (UFG) structure, Fig. 2d. In this regard, particle interior regions are characterized by large grains with high dislocation density. Fig. 2c shows a TEM image of a particle/particle boundary region, which contains pancake structures, comprising thin micro-bands (MBs), several hundreds of nanometers in length. These MBs, in some cases, are subdivided into smaller pancaked grains, small pancake-shaped cells (SPCs [17,21]), by low angle grain boundaries (LAGBs). Another common observation in particle–particle interface regions is the presence of UFG structures (Fig. 2d), which develop due to dynamic and/or static recrystallization. This restoration phenomenon occurs in particle–particle interface regions due to the large plastic strain and elevated temperatures ($>200\text{ }^{\circ}\text{C}$) experienced during cold spray

processing. A detailed mechanistic discussion of the various microstructural features observed in each of these regions of the CSP sample has been reported elsewhere [12].

3.3. Microstructure evaluation — CSP deposition in annealed condition

Fig. 3 shows bright and dark field TEM montage images of the CSP sample after annealing to 450 $^{\circ}\text{C}$ with a heating rate of 10 $^{\circ}\text{C}/\text{min}$. From inspection of Fig. 3a, the annealing process provided sufficient thermal driving force for recovery and recrystallization, resulting in the loss of much of the stored energy. The grains are equiaxed with well-defined, straight GBs, unlike the inhomogeneous microstructure observed in the as-deposited coating (Fig. 2). Furthermore, close inspection of grain interiors reveals that many of the grains are free of dislocations (limited diffraction contrast) and residual stress has been relieved through the annealing process. Conversely, some grains still contain a medium dislocation density evidenced by the somewhat banded contrast in the dark field image (Fig. 3b).

Fig. 4 shows the microstructure of the particle–particle interface and particle interior regions of the annealed CSP sample after annealing. Particle interior regions, Fig. 4a, appear to still have significant dislocation density and therefore these regions did not undergo full recovery during the annealing process. This phenomenon is likely due to the presence of a high density of fine precipitates in the grain interiors, which tend to pin dislocations, hindering rapid dislocation migration [21,38–40]. Fig. 4b shows a particle–particle interface region, which in as-deposited condition, contained pancaked grain structures (Fig. 2c). In these regions, the microstructure experienced significant recrystallization during the annealing process, developing an UFG structure as opposed to a pancaked structure (Fig. 2c). Finally, particle–particle interface regions, originally characterized by UFG structures in the as-deposited state, appear relatively unaffected by the annealing process. Although subtle, these regions showed some reduction in overall dislocation density, improved GB definition, and some evidence of recrystallization. It is important to note that limited, if any, grain growth was observed in any region of the microstructure during the annealing process. This is attributed to the presence of extensive GB solute segregation in the as-deposited microstructure, which may lead to nucleation of numerous precipitates at GBs during annealing. Solute segregation in as-deposited CSP coatings has been reported in multiple studies [12,17,25–27]. Furthermore, Wert et al. [41] suggested small GB precipitates may lead to retarded grain growth in 7xxx Al alloys due the Zener effect. Wang et al. [42] and Aust et al. [43] have also shown that even small average solute concentrations result in a dramatic reduction in GB migration. As a result, it is rational that limited grain growth was observed after annealing of the CSP sample. It should also be noted that the total annealing time in this study is somewhat limited and it is expected that grain growth would occur if the annealing time was increased substantially.

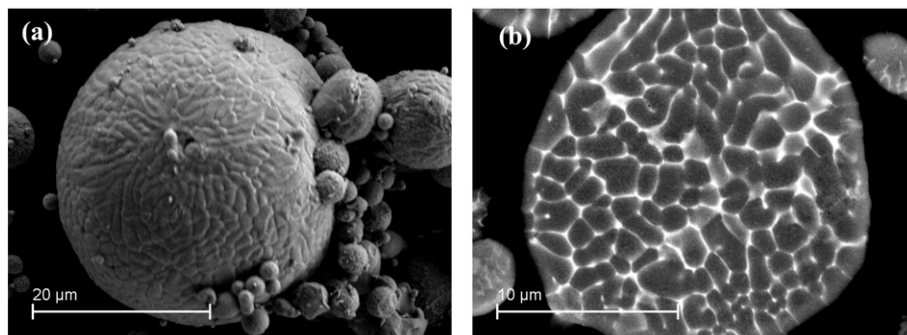


Fig. 1. SEM micrographs of gas-atomized 7075 Al powder showing (a) external surface of a typical powder particle and (b) BSE image cross-section of a typical powder particle.

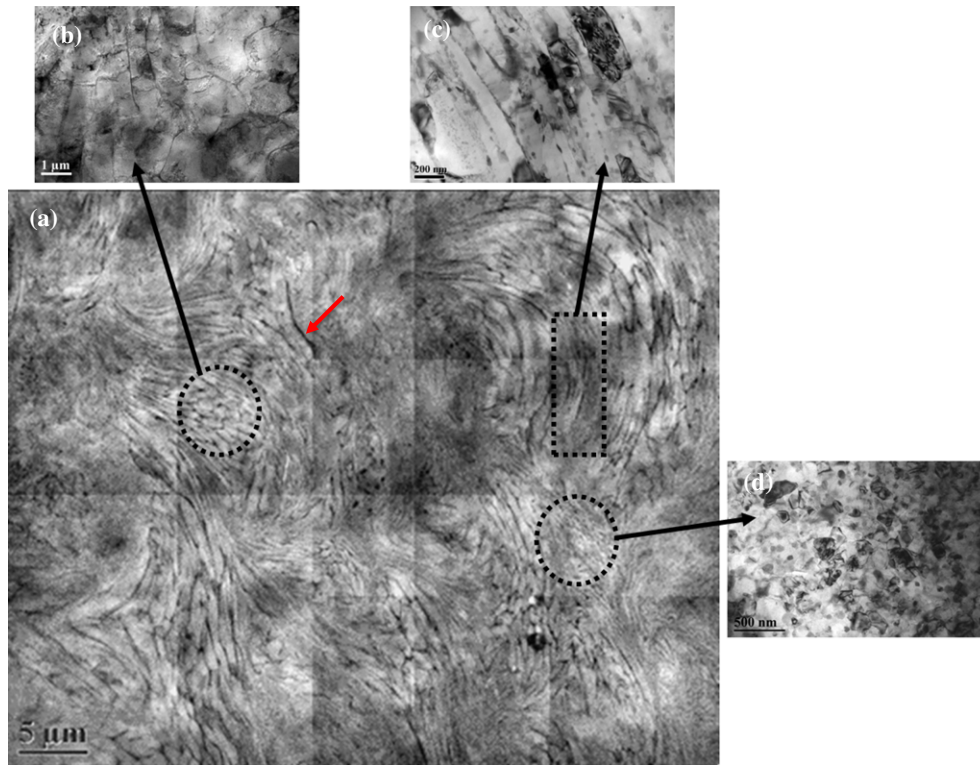


Fig. 2. (a) STEM montage image showing the microstructure of the CSP 7075 deposit, (b) TEM image of particle interior region, (c) TEM micrograph obtained from a particle/particle region revealing a pancaked structure, and (d) TEM micrograph obtained from a particle/particle interface region revealing a UFG structure. The red arrow in (a) shows an elongated interparticle void.

3.4. Non-isothermal annealing of the CSP deposition

3.4.1. Thermal analysis

Fig. 5 shows DSC curves from the as-received powder (ARP) and CSP samples obtained while heating the specimens to 450 °C at a rate of 10 °C/min. Both the ARP and the CSP samples show similar behavior,

characterized by three distinct regions (i.e. Regions I, II, and III) associated with the formation or dissolution of precipitates in the CSP sample microstructure during heating. In this regard, the precipitate sequence (from a supersaturated solid solution) is well-known and follows three primary steps: (1) formation of small (~5–10 nm) Guinier–Preston (G–P) zones, (2) formation of semicoherent, hexagonal, metastable MgZn_2 precipitates

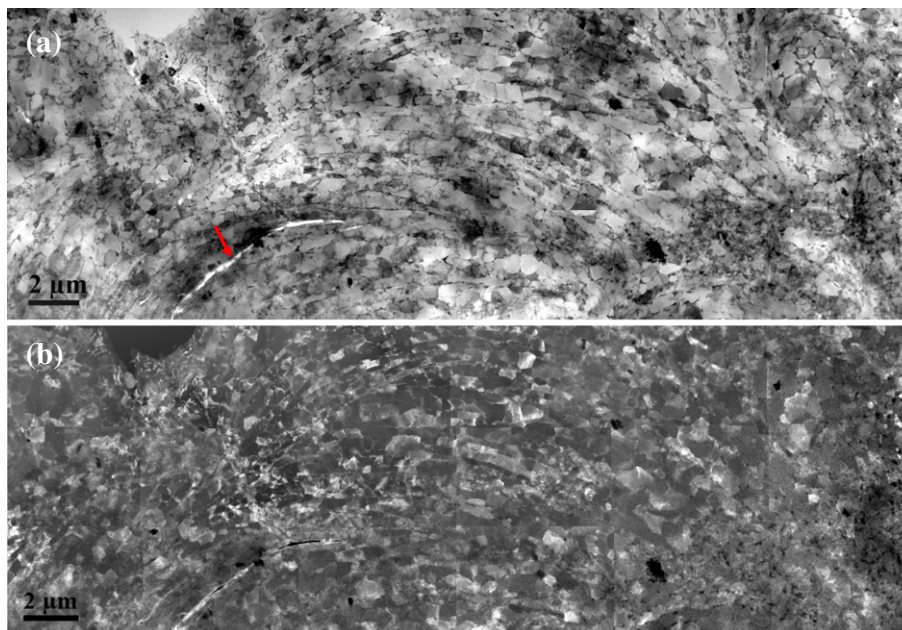


Fig. 3. Bright field (a) and dark field (b) montage TEM images obtained from the CSP 7075 deposition after annealing to 450 °C. The red arrow shows an elongated void between two particles.

(η'), and (3) formation of incoherent, hexagonal, equilibrium MgZn_2 precipitates (η). From inspection of Fig. 3, Region I is characterized by a low temperature endothermic reaction, typically associated with the dissolution of Guinier–Preston (G–P) zones. Region II corresponds to an intermediate temperature exothermic reaction, associated with the formation of η' and η precipitates. Finally, Region III corresponds to a high temperature endothermic region, attributed to the dissolution of η' and η precipitates [22,23,44–47]. While both DSC curves (i.e. ARP and CSP samples) are characterized by the three regions above, there are some subtle differences in behavior between the two samples.

In Region I, the DSC curve for the CSP sample has a somewhat shallow endothermic peak as compared to the more distinct peak in the ARP

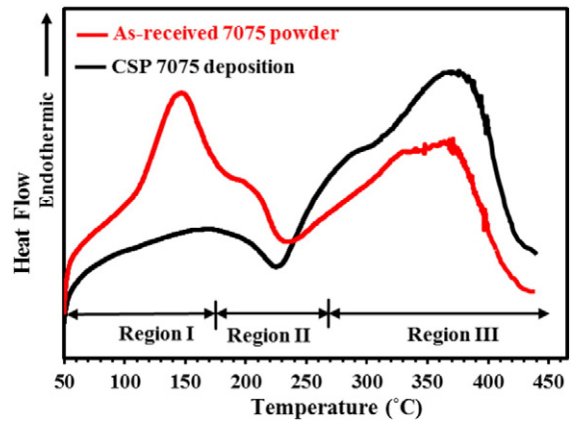


Fig. 5. DSC scans of the CSP 7075 deposition (black line) and the as-received powder (red line) during heating to 450 °C at a rate of 10 °C/min.

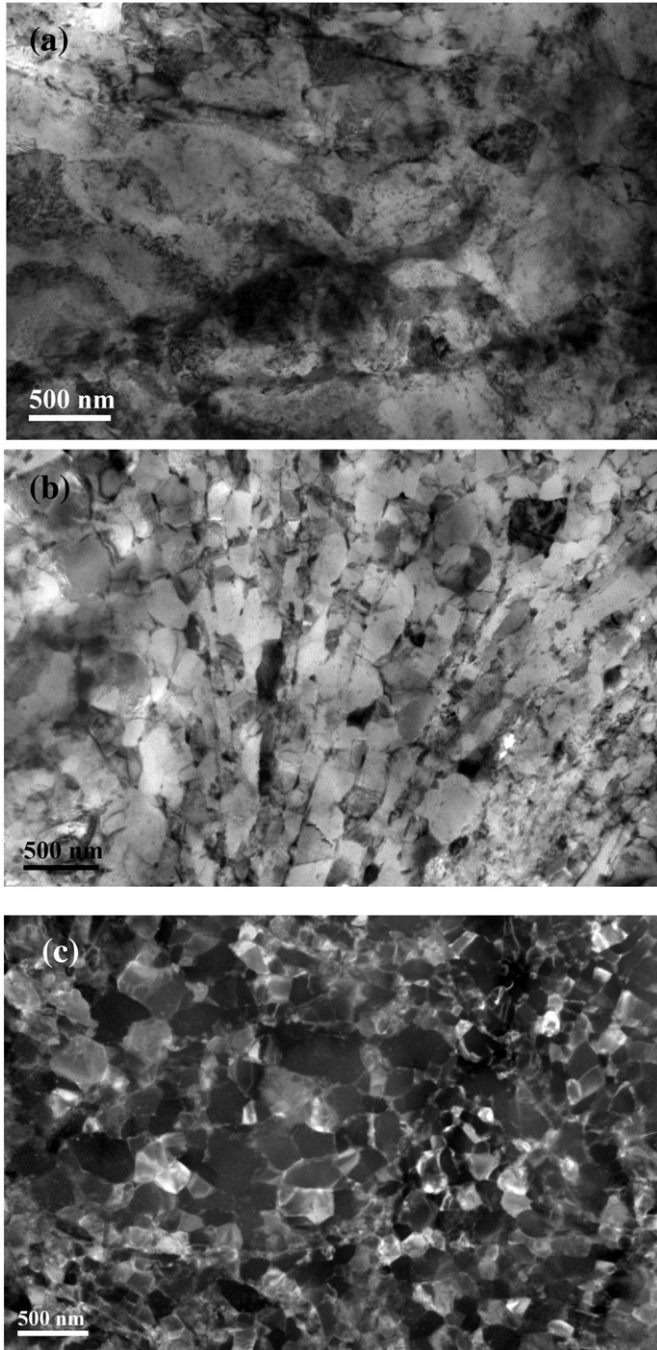


Fig. 4. TEM micrographs obtained from different regions in the CSP 7075 deposition after annealing to 450 °C, including (a) particle interiors, (b) particle/particle interfaces with the pancaked structures, and (c) particle/particle interfaces with UFG structure.

sample. This result suggests that the volume fraction of G–P zones in the powder sample is larger than that in the CSP sample. It is likely that significant plastic strain experienced by the CSP sample during cold spray deposition has resulted in the transformation of G–P zones to metastable η' precipitates. Gubicza et al. [23] showed an absence of G–P zones and significant volume fraction of η'/η precipitates in Al–Mg–Zn alloys processed by equal-channel angular pressing (ECAP) at 200 °C. The authors attributed the formation of η'/η precipitates to the high dislocation density in the processed microstructure, where dislocations act as nucleation sites for η precipitates. In contrast, Zhao et al. [22] observed a higher volume fraction of G–P zones and lower volume fraction of η' precipitates in ultra-fine grained 7075 alloys subjected to ECAP at room temperature and subsequently naturally aged, as compared to conventional grained, unprocessed material. The primary difference between these findings is the application of ECAP with and without in-situ heating (200 °C). Thus, it is likely that rapid η'/η precipitate nucleation at dislocations is promoted by increased temperature, permitting increased diffusion of alloying elements along dislocation cores. In the case of cold spray processing, both high dislocation density [3–5,12,17] and elevated temperature (i.e. >300 °C) [47–49] are present. Thus, it is likely that the low volume fraction of G–P zones in the CSP sample is due to precipitation of η'/η precipitates at dislocations in the deformed microstructure. Furthermore, the DSC curve of the ARP sample shows a shoulder at the end of the G–P zone dissolution peak, which was caused by the dissolution of some of η' phase [22,44]. This observation is common in naturally aged 7075 Al alloys [45,46].

In Region II, the ARP sample shows a deeper exothermic peak as compared to the CSP sample, indicating a higher volume fraction of η'/η phases formed during DSC heating. This is a logical result considering the higher volume fraction of newly dissolved G–P zones (precursors for η'/η precipitation) in the ARP sample and larger volume fraction of pre-existing η'/η precipitates in the CSP sample. Furthermore, the peak temperature (~225 °C) for the exothermic peak in the CSP sample is roughly 10 °C lower than that for the ARP sample (~235 °C). This demonstrates that cold spray processing accelerates η'/η precipitation, which is in agreement with other SPD processes [22,23,45]. Once again, accelerated precipitation in CSP samples is attributed to a high density of dislocations and LAGBs in cold spray deposited material [12,34], which act as potential nucleation sites for the intermediate precipitates.

As aforementioned, Region III is characterized by an endothermic peak associated with the dissolution of η'/η precipitates in the microstructure. As expected, the endothermic peak is larger for the CSP sample than the ARP sample, indicating the presence of more precipitates in the deposited material. Also, it is interesting to note that the CSP sample shows a shoulder in the beginning (~290 °C) of this region. Richard and Adler [50] suggested this shoulder is a consequence of η precipitate

growth by an Ostwald ripening mechanism during the initial stages of dissolution.

3.4.2. Phase analysis

XRD analysis was performed to determine the phases present in the microstructure at critical temperatures identified during DSC analysis. For this purpose, samples were excised from the CSP sample and heated to the specified temperature at a rate of 10 °C/min (matching that for DSC). Fig. 6 shows the resultant XRD patterns. Inspection of the room temperature (RT) pattern shows several weak peaks near $2\theta = 20^\circ$. These peaks are associated with the η' phase [22,23,44,51,52], demonstrating the presence of η' precipitates in the as-deposited material. With increasing annealing temperature to 120 °C, peaks representative of η'/η precipitates become more apparent (e.g. peaks between $2\theta = 38^\circ$ to 45°) in the XRD pattern. Thus, it is likely that the shallow Region I peak observed in the CSP sample DSC curve (Fig. 5) is due to the exothermic reaction associated with early η'/η precipitation, in addition to limited G–P zone dissolution (endothermic). It is clear that increasing temperatures up to 280 °C results in an increased intensity of η'/η phase peaks, representing the continued precipitation of these phases in Region II. After 280 °C, corresponding to the beginning of Region III, the intensity of η'/η peaks start to become weaker, signifying the dissolution of these phases back into the matrix. Thus, the XRD analysis confirms the observations made through DSC analysis. Finally, at 450 °C the XRD pattern is free of strong diffraction peaks, aside from those for aluminum, indicating the dissolution of nearly all precipitates in the microstructure and formation of a solid solution.

3.4.3. Microstructure evolution during non-isothermal annealing

In-situ TEM heating was used to observe the microstructural evolution during the full annealing cycle from room temperature to 450 °C (heating rate of 10 °C/min). This analysis was restricted to particle/particle boundary regions of the CSP sample, as these regions experienced the most microstructural changes during initial annealing evaluations (Fig. 3). All of the observed microstructural changes, e.g. dislocation movement, recovery, precipitation and recrystallization, and their approximate temperatures, were recorded and can be viewed in the Supplementary Movie File (Video). The time lapse movie is made up of roughly 420 TEM images that were captured every 7 s. In this way, the temperatures at which real microstructural changes began could be observed. Figs. 7 and 8 show TEM micrographs obtained from the CSP sample at selected temperatures (corresponding to critical temperatures from DSC analysis) in the annealing process. Also, for better

comparison of the microstructures at these temperatures, the grain size (Fig. 9a), microstrain (Fig. 9b), dislocation density (Fig. 10a), and lattice parameter (LP) (Fig. 10b) are reported for each critical temperature. In this regard, dislocation densities were calculated using grain size (d) and microstrain (ϵ) estimates provided by XRD analysis. Here the dislocation density, ρ , is given by Eq. (3)[22,24]:

$$\rho = \frac{2\sqrt{3}\epsilon}{db}, \quad (3)$$

where b is the magnitude of the Burgers vector for Al (0.286 nm) [33]. This relationship (Eq. (3)) is commonly used when studying aluminum alloys subjected to severe plastic deformation [22,24]. In this context, cold spray processing can be considered a severe plastic deformation process, considering the high strain rates (approaching 10^9 s^{-1}) [11,17,26] experienced by the material during deposition. Thus, it is rational to use Eq. (3) for estimation of dislocation density in this study.

Fig. 7a shows a TEM micrograph of the CSP sample at room temperature (i.e. as-deposited condition). The microstructure has been discussed in Section 3.2 and is characterized by a high dislocation density, pancake structures, and some indications of UFG structures. After annealing to 120 °C, it is apparent that some level of recovery has initiated whereby dislocation rearrangement is observed. In fact, although not discernable in still images, the Supplemental Video File (Video) demonstrates the movement of dislocations at temperatures as low as 70 °C. Fig. 10a, however, shows that a measurable change in dislocation density was not observed at this low temperature (120 °C). Furthermore, a slight decrease in microstrain was observed at 120 °C, likely associated dislocation rearrangement in the absence of significant reduction in dislocation density. Finally, there was no evidence of grain growth (Fig. 9a) as boundary mobility is very low at this temperature. Two important observations may be made from inspection of Fig. 9a. First, grain length (~525 nm), determined by TEM analysis, is roughly twice that of grain width (~250 nm). This once again demonstrates the presence of elongated grains (pancake structures) in the microstructure. Also, Fig. 9a shows a discrepancy between grain size measured by TEM and XRD analyses (XRD providing lower grain size estimates). This is a well-known phenomena in samples which have experienced severe plastic deformation and occurs because the XRD method estimates the coherent diffraction domain size (crystallite size), incorporating both sub-grain and dislocation cell structures into the estimate [22,23]. Thus, grain size estimates are smaller than those obtained by direct TEM image analysis.

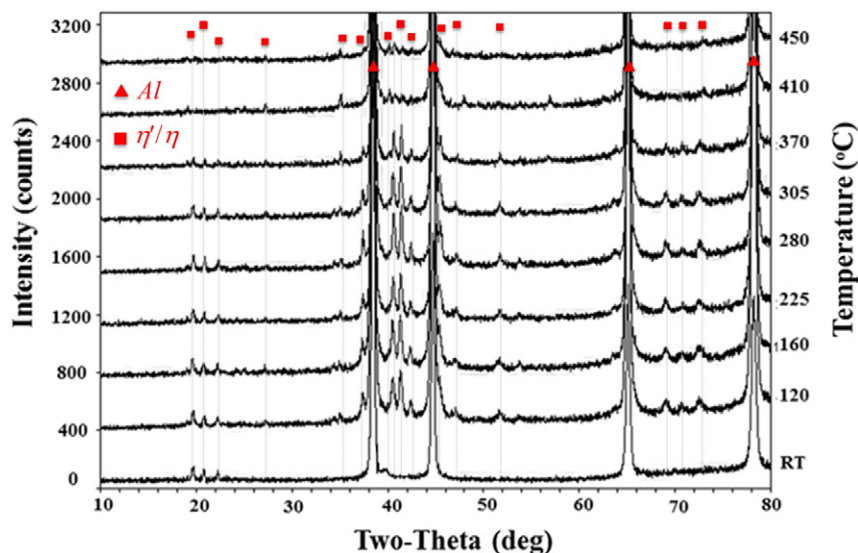


Fig. 6. XRD patterns of the CSP 7075 deposition subjected to non-isothermal annealing at various temperatures between RT and 450 °C. The heating rate for all samples was 10 °C/min.

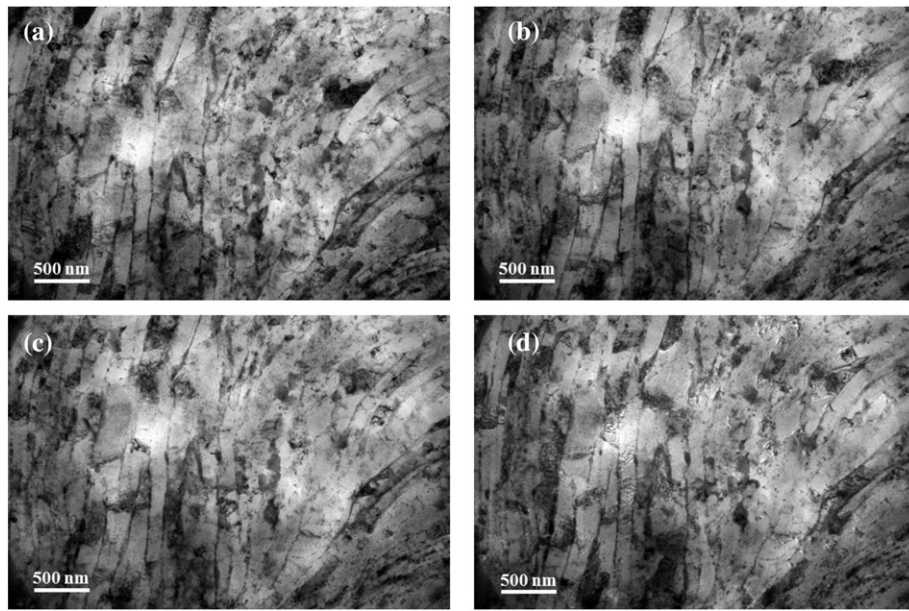


Fig. 7. TEM images from the annealed CSP 7075 deposition at various temperatures including (a) RT (no annealing), (b) 120 °C, (c) 160 °C, and (d) 225 °C.

Upon further heating to 160 °C, continued evidence of recovery was observed in the microstructure (Fig. 7c), attributed to pronounced dislocation movement. As such, a slight decrease in dislocation density

was observed (Fig. 10a) in conjunction with a reduction in microstrain (Fig. 9b). Once again, no change in average grain size was observed. A noticeable increase in lattice parameter (LP) was observed upon heating

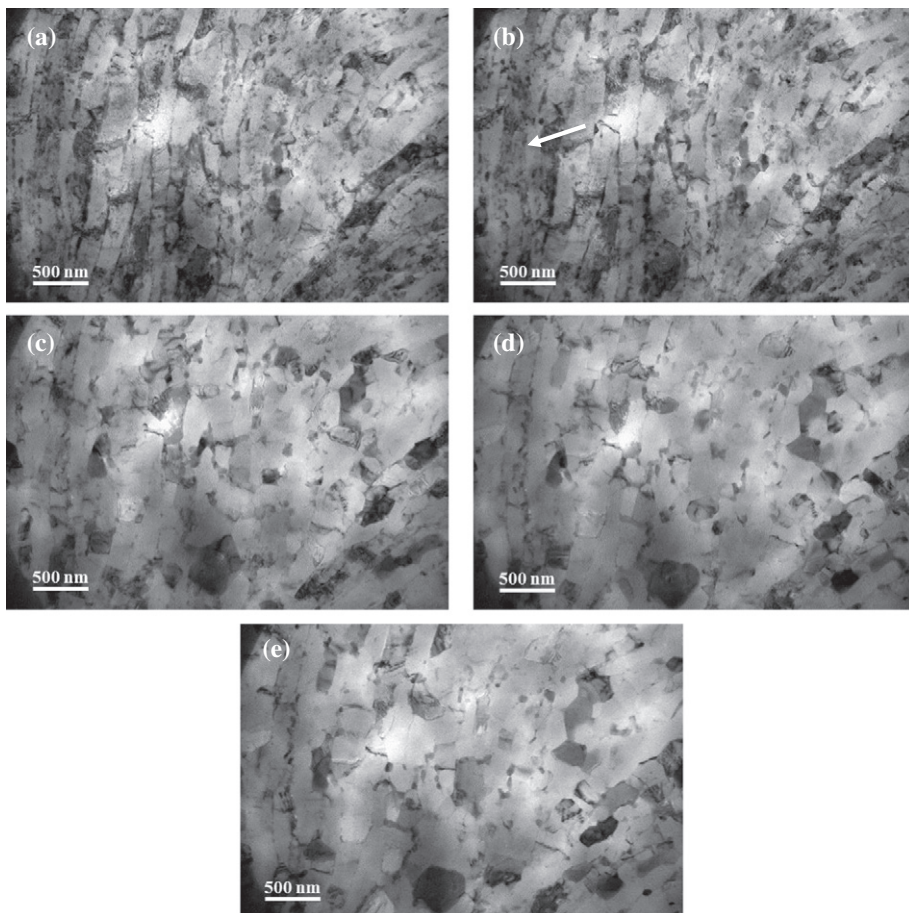


Fig. 8. TEM images from the annealed CSP 7075 deposition at various temperatures including (a) 280 °C, (b) 305 °C, (c) 370 °C, (d) 410 °C, and (e) 450 °C.

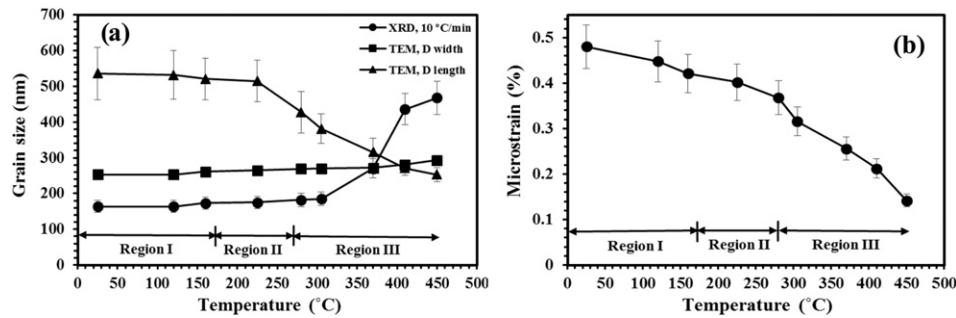


Fig. 9. a) Grain size evolution of the CSP 7075 Al deposition after annealing to various temperatures, as measured by XRD (circles) and TEM (squares and triangles) techniques, b) Microstrain evolution of the CSP 7075 Al deposition after annealing to various temperatures, as measured by XRD peak broadening analysis [24].

between 120 °C and 160 °C (Fig. 10b). This is due to the dissolution of G–P zones in this temperature range, corresponding with DSC analysis (Region I, Fig. 5).

Fig. 7(d) shows the microstructure of the annealed CSP sample at 225 °C. From inspection of Fig. 7d, the pancaked structure remains stable through this temperature range. This is likely the result of significant GB solute segregation and GB precipitates in the CSP sample [12,34], which hinders GB migration by exerting a drag force on migrating grain or subgrain boundaries. At 225 °C, the formation of η' precipitates has led to a significant decrease in LP (Fig. 10b). Fig. 7d also shows that several grains have experienced a significant decrease in dislocation density (some appear dislocation-free). This is in agreement with the substantial drop in dislocation density from 160 to 225 °C in Fig. 10a.

At 280 °C, the pancaked structure (elongated grains) begins to collapse (Fig. 8a) resulting in a decrease in the average grain length from 536 ± 27 nm at RT to 428 ± 41 nm (Fig. 9a). From inspection of Fig. 8a, and the Supplementary Movie File, the collapse occurs primarily in the horizontal direction of the pancaked structures through the formation of LAGBs. The LAGBs are formed because of free dislocation movement in vertical direction (long axis of pancake grains) during the recovery process. Extensive solute segregation along vertical GBs, however, restricts dislocation movement to the vertical direction of the pancaked grains. As was mentioned before, this segregation is retained from the as-received powder. In addition, extensive plastic deformation which occurs during cold spray processing causes increased segregation along these GBs. SPD-induced grain boundary segregation has been reported in multiple Al alloys, e.g. UFG 6061 alloy processed by CS [53], UFG 6061 alloy processed by HPT [54] and in 7136 alloy processed by ECAP [55]. In summary, during the annealing process, the combination of recovery processes and extensive GB solute segregation results in vertical dislocation movement within the elongated grains, formation of LAGBs, and consequently, leads to the collapse of the pancaked structures.

Further increase in the annealing temperature to 305 °C (Fig. 8b) resulted in continued microstructure recovery (i.e. dislocation annihilation and rearrangement), demonstrated by further decrease in dislocation

density (Fig. 10a). Once again, the grain length continued to decrease, with minor increases in grain width (Fig. 9a). Also, an increase in lattice parameter, owing to the dissolution of η'/η precipitates, is observed in this temperature range (>280 °C). Once again this observation is consistent with DSC analysis results (Region III, Fig. 3).

Fig. 8c and d show that additional heating beyond 370 °C results in pronounced changes in the microstructure. Clearly, significant recrystallization has occurred in this temperature range, evidenced by new equiaxed grains throughout the microstructure. Additionally, a significant decrease in grain boundary precipitates is observed. Thus, it is likely that the dissolution of η'/η precipitates, initiated above 250 °C (Fig. 5), has proceeded to a sufficient degree to improve grain boundary mobility and permit recrystallization. Interestingly, the only region of the microstructure still showing remnants of the as-deposited microband structure (white arrow Fig. 8b) is one in which numerous precipitates have remained at the GBs. From inspection of Figs. 9 and 10, grain length, dislocation density and microstrain values continued to decrease in this temperature range.

The final microstructure, at 450 °C, is shown in Fig. 8e. The microstructure is characterized by a low dislocation density in addition to clearly defined, equiaxed, stress free grains. The microstrain has reached a minimum value. Also, the lattice parameter has increased to ~ 4.056 Å due to a heavy concentration of solute atoms in the aluminum crystal lattice. Fig. 9a demonstrates that the previously elongated grain structure has been transformed such that the grains have an approximate aspect ratio of one (average grain length and width of 254 ± 48 nm and 293 ± 52 nm, respectively). Careful inspection of Fig. 9a, once again shows a discrepancy in grain size estimates between TEM and XRD analysis. In this case, however, XRD analysis resulted in larger estimates of grain size (468 ± 75 nm). The cause of this discrepancy is due to the non-uniform grain size between particle interiors and particle–particle boundaries. The TEM estimates reported in Fig. 9a are restricted to particle–particle boundary regions, while XRD analysis has sampled a much larger volume of material (incorporating both particle interiors and particle–particle boundaries). Thus, at temperatures below ~ 305 °C, significant recrystallization has not occurred, the

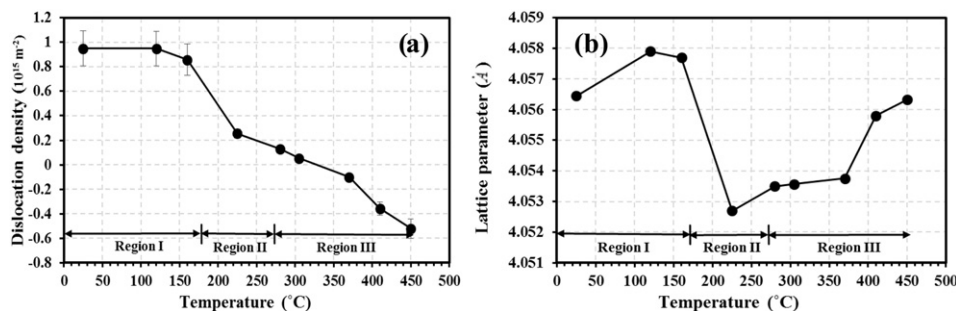


Fig. 10. a) Dislocation density measurements of the CSP 7075 Al deposition after annealing to various temperatures, as determined from XRD analysis [16], b) Lattice parameter variation of the CSP 7075 Al deposition after annealing to various temperatures, as determined from the XRD analysis.

XRD grain size estimate is controlled by the size of subgrain and dislocation cell structures. Above 305 °C, however, extensive recovery has occurred and the estimate is controlled (in large part) by the actual grain size, which happens to be non-uniform in this case. Therefore, similar to results reported in Section 3.2, limited, if any, grain growth was observed during the annealing process. Once again, this is attributed to the presence of extensive GB precipitates in the microstructure, which tends to pin mobile grain boundaries and retard growth. This is an important finding as it provides an indication of the thermal stability of the UFG structure in the CSP sample. The results may provide important insight into the potential for post-deposition heat treatments, used to improve mechanical properties, for this material.

3.4.4. Microhardness measurements

Microhardness measurements were also performed to study the effect of non-isothermal annealing, and associated microstructural changes, on the mechanical properties of the CSP sample. To evaluate this effect, samples were excised from the CSP 7075 Al deposition, then heated (10 °C/min) to critical temperatures identified during microstructural evaluation, and subsequently quenched to RT. Annealed specimens were then subjected to Vickers microhardness testing. Fig. 11 shows the microhardness measurements obtained from the CSP 7075 Al deposition samples following non-isothermal annealing to various temperatures between RT (no annealing) and 450 °C. From inspection of Fig. 11, the microhardness of the CSP sample decreased slightly between RT and 140 °C (Region I). This decrease in hardness is attributed to the dissolution of G–P zones in this temperature range. In Region II (160 °C and 225 °C samples), the microhardness increased due to precipitation strengthening which occurred due to a high volume fraction of newly precipitated η'/η phases. This is an expected result as η'/η are the primary strengthening phases in 7075 Al alloys.

In Region III, the hardness values first decreased, as expected, due to dissolution of η'/η phases. At temperatures above 370 °C, however, the hardness increased with increasing annealing temperature, eventually exceeding the peak hardness obtained in Region II. This is a surprising result considering the limited number of η'/η precipitates (see Fig. 6) and low dislocation density (see Fig. 10a) at these temperatures. As a comparison, the microhardness of conventional 7075 Al alloy, solution treated and annealed as described above, was also measured and is reported in Fig. 11. As expected, the conventional 7075 Al alloy showed a peak hardness in Region II (160 °C and 225 °C) followed by a rapid decrease in hardness with increasing annealing temperature (up to 450 °C). This change in microhardness with annealing temperature is primarily due to the formation (Region II) and subsequent dissolution (Region III) of η'/η precipitates. Some grain growth (average grain size at RT and after 450 °C annealing was 40 ± 11 and 100 ± 23 μm , respectively), determined by optical metallography, was also observed in the

conventional 7075 Al alloy sample, which may have played a limited role in the reduction in hardness at high temperatures. Thus, the CSP sample shows significantly different microhardness behavior during non-isothermal annealing as compared to conventional 7075 Al. It is important to isolate the cause of this discrepancy.

In this regard, there are four strengthening mechanisms that may play a role in the microhardness evolution of this material during non-isothermal annealing: grain boundary strengthening, solid solution strengthening, precipitate strengthening, and strain hardening. Prior to annealing, the grain size of the CSP samples (~ 500 nm, Fig. 9a) was much smaller than the conventional 7075 Al samples (40 ± 11 μm , measured by optical metallography). Furthermore, the dislocation density (representative of strain hardening) in the CSP deposit is expected to be much higher than that of the solution treated 7075 Al specimens. Additionally, considering the similarity in the thermal history of the CSP and conventional 7075 Al samples, it is expected that the degree of solid solution and precipitate strengthening is not substantially different. With these observations in mind, it is surprising that the conventional 7075 Al samples shows higher hardness than the CSP samples for all annealing temperatures between RT and 225 °C (Fig. 11). There is one additional factor, however, that can have a significant impact on mechanical properties of cold spray deposited material: porosity. It is well known that the presence of porosity and triple junction voids, found primarily at particle–particle boundaries, can have a significant detrimental impact on mechanical properties (i.e. tensile strength, ductility, hardness) [34–37]. In this regard, Fig. 2 shows some degree of porosity in the as-deposited microstructure. Furthermore, previous studies have demonstrated an increase in hardness, compared to as-deposited cold spray specimens, with increasing annealing temperature, attributed to a decrease in inter-particle porosity [12,34]. Thus, it is likely that the low hardness (compared to conventional 7075 Al) of the cold spray deposition at temperatures below 225 °C is due to inter-particle porosity in the CSP samples. The increase in hardness with increasing annealing temperatures beyond 370 °C is most likely due to the removal or healing of inter-particle porosity. Furthermore, the much higher hardness observed in the cold spray deposition compared to the conventional 7075 Al sample at high temperatures (above 370 °C) is likely due (primarily) to grain boundary strengthening. At these temperatures, η'/η precipitates dissolved into the aluminum matrix and dislocation density has dropped dramatically thereby limiting the effect of precipitate strengthening and strain hardening, respectively. Furthermore, although the concentration of solute atoms in the aluminum matrix has increased, resulting in an increase in lattice parameter and local strain energy, it is unlikely that the solid solution strengthening effect would be substantially different between the CSP and conventional 7075 Al samples.

To justify the conclusion that grain boundary strengthening is the primary driver for the deviation in hardness at high temperatures, the grain boundary strengthening effect was estimated. As was shown in Fig. 7, the grain size of the CSP 7075 Al deposition remained small (~ 500 nm) when annealing beyond 370 °C and this was attributed to the pinning effect of GB precipitates and solute segregation. In the conventional 7075 Al sample, however, some grain growth was observed during annealing and the final grain size was 100 ± 23 μm (versus 40 ± 11 μm at RT). This difference in grain size can lead to a significant hardness difference between the annealed CSP and conventional 7075 Al samples. In this regard, the degree of grain boundary strengthening was estimated using the Hall–Petch equation [24,56–58]:

$$\sigma_y = \sigma_0 + \frac{k_y}{\sqrt{d}}, \quad (4)$$

where d is the average grain diameter, σ_0 is the friction stress, and k_y is the Hall–Petch slope.

According to previous studies in UFG Al–Zn–Mg alloys [24,57], k_y is equal to $0.12 \text{ MPa}/\sqrt{\text{m}}$. Since σ_0 is a constant, applying the mean

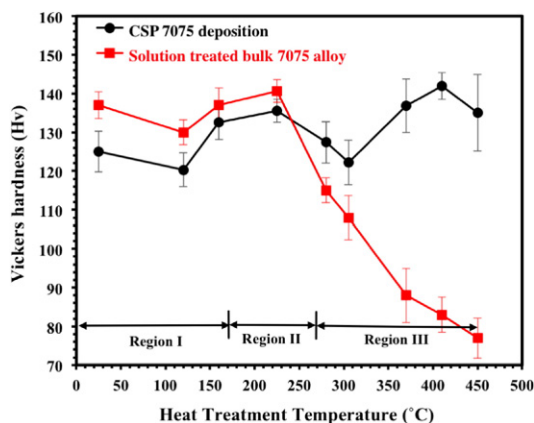


Fig. 11. Vickers microhardness measurements obtained from the CSP 7075 Al and conventional 7075 Al alloy samples after annealing at various temperatures.

grain size in the annealed CSP and conventional 7075 Al samples results in a 160 MPa yield strength difference between these two materials. For comparison, the hardness values in Fig. 11 were converted to yield strength. For this purpose, the simple relationship between Vickers hardness (HV) and yield strength ($HV \times 3 \approx \sigma_y$) was used. This equation has been widely used in the literature for various polycrystalline metals and alloys, e.g. Cu [59], stainless steel [60], nanocrystalline Ni and Co [61], nanocrystalline Cu [62], Zn [63], and Pd [64]. Using this technique, the values of 425 and 240 MPa were obtained for the yield strength of the annealed CSP and bulk 7075 Al alloy, respectively. Thus the net difference in estimated yield strength is 185 MPa, which is reasonably close to the difference calculated from Hall–Petch equation (160 MPa). These estimates indicate that the primary strengthening mechanism responsible for higher hardness in annealed (above 370 °C) CSP specimens, compared to that of conventional 7075 Al samples, is grain boundary strengthening.

Overall, the analysis reveals that hardness of the CSP samples is influenced by precipitation hardening, grain boundary strengthening, and inter-particle porosity. When subjected to low temperature (<370 °C) annealing, inter-particle porosity tends to reduce the hardness of the highly deformed CSP material. Annealing the CSP material beyond 370 °C results in a diminished influence of inter-particle porosity, likely due to the reduction of porosity at higher temperatures, and increased influence of grain boundary strengthening arising from the retention of a UFG structure. This is in good agreement with previous studies [35–37,65–68] that showed that annealing at high temperatures can recover the loss of ductility in the deposited materials by reducing the porosity in the microstructure.

4. Conclusions

This study investigates the relationship between microstructure and mechanical properties of CSP 7075 Al depositions during non-isothermal annealing from RT to 450 °C. The as-deposited CSP samples were characterized by three distinct regions: (1) particle interior regions; (2) particle–particle interface regions containing pancake grain structures; and (3) particle–particle interface regions containing an ultra-fined grain (UFG) structure. TEM analysis showed that Region (1) and Region (3) above experienced a general decrease in dislocation density during annealing to 450 °C with few other drastic microstructural changes. Limited, if any, grain growth was observed in any region of the microstructure during the annealing process and was attributed to the presence of GB solute segregation and precipitates. In particle–particle interface regions, which contained pancake grain structures (elongated grains), however, substantial microstructural changes were observed and studied in greater detail.

Here DSC analysis revealed that cold spray deposition accelerated the precipitation kinetics in comparison to the as-received powder, however, the overall precipitation sequence was unchanged. Furthermore, XRD and DSC analyses revealed that the CSP results in the precipitation of η'/η precipitates in the as-deposited material, limiting the volume fraction of G–P zones in the microstructure. This observation was attributed to the high dislocation density in the CSP material and elevated temperatures (<300 °C) achieved during deposition.

As expected, the measured dislocation density and microstrain in the microstructure decreased with increasing annealing temperature, an indication of recovery and recrystallization processes within the microstructure. Annealing beyond 370 °C resulted in the recrystallization of the deformed microstructure and a break-up of the pancake grain structure and formation of a more equiaxed UFG structure. Microhardness evaluation revealed the hardness of the CSP material was lower than conventional 7075 Al alloy sample when annealed at low temperatures (below 370 °C), due to the presence of porosity in the CSP material. Annealing beyond 370 °C, however, resulted in substantially higher hardness of the CSP sample. This observation was attributed to grain boundary strengthening arising from the good thermal stability of

the UFG structure within the CSP sample and reduction in inter-particle porosity at these temperatures.

Supplementary data to this article can be found online at <http://dx.doi.org/10.1016/j.surfcoat.2015.07.016>.

References

- [1] H. Assadi, F. Gärtner, T. Stoltenhoff, H. Kreye, *Acta Mater.* 51 (2003) 4379–4394.
- [2] T. Stoltenhoff, H. Kreye, H.J. Richter, *J. Therm. Spray Technol.* 11 (2002) 542–550.
- [3] K. Balani, A. Agarwal, S. Seal, J. Karthikeyan, *Scr. Mater.* 53 (2005) 845–850.
- [4] Y.Y. Zhang, J.S. Zhang, *Mater. Lett.* 65 (2011) 1856–1858.
- [5] G. Bae, K. Kang, J.J. Kim, C. Lee, *Mater. Sci. Eng. A* 527 (2010) 6313–6319.
- [6] M.R. Rokni, C.A. Widener, A.T. Nardi, V.K. Champagne, *Appl. Surf. Sci.* 305 (2014) 797–804.
- [7] M.R. Rokni, C.A. Widener, V.R. Champagne, *Appl. Surf. Sci.* 290 (2014) 482–489.
- [8] T. Stoltenhoff, C. Borchers, F. Gärtner, H. Kreye, *Surf. Coat. Technol.* 200 (2006) 4947–4960.
- [9] T. Schmidt, F. Gärtner, H. Assadi, H. Kreye, *Acta Mater.* 54 (2006) 729–742.
- [10] G. Bae, J.I. Jang, C. Lee, *Acta Mater.* 60 (2012) 3524–3535.
- [11] Y. Zou, D. Goldbaum, J.A. Szpunar, S. Yue, *Scr. Mater.* 62 (2011) 395–398.
- [12] M.R. Rokni, C.A. Widener, G.A. Crawford, *Surf. Coat. Technol.* 251 (2014) 254–263.
- [13] R. Ghelichi, D. MacDonald, S. Bagherifard, H. Jahed, M. Guagliano, B. Jodoin, *Acta Mater.* 60 (2012) 6555–6561.
- [14] Q. Wang, K. Spencer, N. Birbilis, M.X. Zhang, *Surf. Coat. Technol.* 205 (2010) 50–56.
- [15] C. Borchers, F. Gärtner, T. Stoltenhoff, H. Kreye, *J. Appl. Phys.* 96 (2004) 4288–4292.
- [16] Y. Zou, W. Qin, E. Irissou, J.G. Legoux, S. Yue, J.A. Szpunar, *Scr. Mater.* 61 (2009) 899–902.
- [17] M.R. Rokni, C.A. Widener, V.R. Champagne, *J. Therm. Spray Technol.* 23 (2014) 514–524.
- [18] W.B. Choi, L. Li, V. Luzin, R. Neiser, T. Gnäupel-Herold, H.J. Prask, S. Sampath, A. Gouldstone, *Acta Mater.* 55 (2007) 857–866.
- [19] R.Z. Valiev, Y. Gertsman, O.A. Kaibyshev, *Phys. Status Solidi A* 97 (1986) 11–56.
- [20] A.A. Nazarov, A.E. Romanov, R.Z. Valiev, *Acta Metall.* 41 (1993) 1033–1040.
- [21] F.J. Humphreys, M. Hatherly, *Recrystallization and Related Annealing Phenomena*, 2nd ed. Pergamon Press, Oxford, 2004.
- [22] Y.H. Zhao, X.Z. Liao, Z. Jin, R.Z. Valiev, Y.T. Zhu, *Acta Mater.* 52 (2004) 4589.
- [23] J. Gubicza, I. Schiller, N.Q. Chinh, J. Illy, Z. Horita, T.G. Langdon, *Mater. Sci. Eng. A* 460–461 (2007) 77–85.
- [24] K. Ma, H. Wen, T. Hu, T.D. Topping, D. Isheim, D.N. Seidman, E.J. Lavernia, J.M. Schoenung, *Acta Mater.* 62 (2014) 141–155.
- [25] L. Ajdelsztajn, B. Jodoin, P. Richer, E. Sansoucy, E.J. Lavernia, *J. Therm. Spray Technol.* 15 (2006) 495–500.
- [26] L. Ajdelsztajn, A. Zúñiga, B. Jodoin, E.J. Lavernia, *Surf. Coat. Technol.* 201 (2006) 2109–2116.
- [27] Y.Y. Zhang, X.K. Wu, H. Cui, J.S. Zhang, *J. Therm. Spray Technol.* 20 (2011) 1125–1132.
- [28] L. Kunz, P. Lukáš, M. Svoboda, *Fatigue strength, Mater. Sci. Eng. A* 424 (2006) 97–104.
- [29] S.K. Panigrahi, R. Jayaganthan, *J. Mater. Sci.* 45 (2010) 5624–5636.
- [30] D.H. Shin, B.C. Kim, K.T. Park, W.Y. Choo, *Acta Mater.* 48 (2000) 3245–3252.
- [31] H. Wen, T.D. Topping, D. Isheim, D.N. Seidman, E.J. Lavernia, *Acta Mater.* 61 (2013) 2769.
- [32] G.K. Williamson, W.H. Hall, *Acta Metall.* 1 (1953) 22.
- [33] A.C. Hall, D.J. Cook, R.A. Neiser, T.J. Roemer, D.A. Hirschfeld, *J. Therm. Spray Technol.* (2006) 233–238.
- [34] M.R. Rokni, C.A. Widener, G.A. Crawford, M.K. West, *Mater. Sci. Eng. A* 625 (2015) 19–27.
- [35] Z. Li, X. Yang, J. Zhang, B. Zheng, Y. Zhou, A. Shan, E.J. Lavernia, *Metall. Mater. Trans. A* 45 (2014) 5017–5028.
- [36] G. Sundararajan, N.M. Chavan, G. Sivakumar, P.S. Phani, *J. Therm. Spray Technol.* 19 (2010) 1255–1266.
- [37] B. Al-Mangour, P. Vo, R. Mongrain, E. Irissou, S. Yue, *J. Therm. Spray Technol.* 23 (2014) 641–652.
- [38] D. Zhang, M. Suzuki, K. Maruyama, *Scr. Mater.* 52 (2005) 899–903.
- [39] M.R. Rokni, A. Zarei-Hanzaki, H.R. Abedi, *Mater. Sci. Eng. A* 532 (2012) 593–600.
- [40] M.R. Rokni, A. Zarei-Hanzaki, A.A. Roostaei, H.R. Abedi, *Mater. Des.* 32 (2011) 2339–2344.
- [41] C.C. Bampton, J.A. Wert, M.W. Mahoney, *Metall. Trans. A* 13 (1982) 193.
- [42] N. Ma, S.A. Dregia, Y. Wang, *Acta Mater.* 51 (2003) 3687–3700.
- [43] K.T. Aust, J.W. Rutter, *Trans. AIME* 215 (1959) 119–127.
- [44] W. Lacom, *Thermochim. Acta* 271 (1996) 93–100.
- [45] C.B. Fuller, M.W. Mahoney, M. Calabrese, L. Micono, *Mater. Sci. Eng. A* 527 (2010) 2233–2240.
- [46] J.K. Park, A.J. Ardell, *Mater. Sci. Eng. A* 114 (1989) 197–203.
- [47] T. Schmidt, F. Gärtner, H. Assadi, H. Kreye, *Acta Mater.* 54 (2006) 729–742.
- [48] W.Y. Li, W. Gaob, *Appl. Surf. Sci.* 255 (2009) 7878–7892.
- [49] S. Yin, X. Wang, B.-P. Xu, W.-Y. Li, *J. Therm. Spray Technol.* 19 (2010) 1032–1041.
- [50] D. Richard, P.N. Adler, *Metall. Trans. A* 8 (1977) 1177–1183.
- [51] S.K. Panigrahi, R. Jayaganthan, *Mater. Des.* 32 (2011) 3150–3160.
- [52] S.K. Panigrahi, R. Jayaganthan, *J. Alloys Compd.* 509 (2011) 9609–9616.
- [53] M.R. Rokni, C.A. Widener, S.P. Ahrenkiel, B.K. Jasthi, V.R. Champagne, *Surf. Eng.* 30 (2014) 361–368.
- [54] G. Nurislamova, X. Sauvage, M. Murashkin, R. Islamgaliev, R. Valiev, *Philos. Mag. Lett.* 88 (2008) 459–466.

- [55] G. Sha, L. Yao, X. Liao, S.P. Ringer, Z.C. Duan, T.G. Langdon, *Ultramicroscopy* 111 (2011) 500–505.
- [56] H. Conrad, *Acta Metall.* 11 (1963) 75–77.
- [57] H. Fujita, T. Tabata, *Acta Metall.* 21 (1973) 355–365.
- [58] D.N. Seidman, E.A. Marquis, D.C. Dunand, *Acta Mater.* 50 (2002) 4021.
- [59] L. Lu, R. Schwaiger, Z.W. Shan, M. Dao, K. Lu, S. Suresh, *Acta Mater.* 53 (2005) 2169–2179.
- [60] O. Takakuwa, Y. Kwaragi, H. Soyama, *J. Surf. Eng. Meter. Adv. Technol.* 3 (2013) 262–268.
- [61] I. Brooks, P. Lin, G. Palumbo, G.D. Hibbard, U. Erb, *Mater. Sci. Eng. A* 491 (2008) 412–419.
- [62] G.J. Fan, H. Choo, P.K. Liaw, E.J. Lavernia, *Mater. Sci. Eng. A* 409 (2005) 243–248.
- [63] H. Conrad, J. Narayan, *Acta Mater.* 50 (2002) 5067–5078.
- [64] P.G. Sanders, C.J. Youngdahl, J.R. Weertman, *Mater. Sci. Eng. A* 234–236 (1997) 77–82.
- [65] W.Y. Li, C.J. Li, H. Liao, *J. Therm. Spray Technol.* 15 (2006) 206–211.
- [66] W.Y. Li, C. Zhang, H. Liao, C. Coddet, *J. Coat. Technol. Res.* 6 (2009) 401–406.
- [67] P. Vo, E. Irissou, J.G. Legoux, S. Yue, *J. Therm. Spray Technol.* 22 (2013) 954–964.
- [68] A.C. Hall, D.J. Cook, R.A. Neiser, T.J. Roemer, D.A. Hirschfeld, *J. Therm. Spray Technol.* 15 (2006) 233–238.